Visibility and apparent size of Néel-type magnetic skyrmions in Fresnel defocus images of multilayer films

Supplementary Information

T. Denneulin[1*], J. Caron[1], K. Müller-Caspary[1], O. Boulle[2], A. Kovács[1] and R. E. Dunin-Borkowski[1]

[1] *Ernst Ruska-Centre for Microscopy and Spectroscopy with Electrons and Peter Grünberg Institute, Forschungszentrum Jülich, 52425 Jülich, Germany.*

[2] *Université Grenoble Alpes, CNRS, CEA, Grenoble INP, Spintec, Grenoble, France.*

*email address: t.denneulin@fz-juelich.de

Supplementary Information 1:

Cross-sectional HAADF STEM image and EDX maps

In order to verify the composition of the multilayer stack, a cross-sectional specimen was prepared using a focused Ga^+ ion beam scanning electron microscope (FIB SEM) FEI Helios platform. Scanning transmission electron microscopy (STEM) and energy-dispersive X-ray spectroscopy (EDX) were carried out at 200 kV using an FEI Titan TEM equipped with a Schottky field emission gun, a CEOS probe aberration corrector, a high-angle annular dark-field (HAADF) detector and a Super-X EDX detection system.

Figure S1(a) shows a table of the nominal compositions and thicknesses of the layers, based on calibrated deposition rates. Figure S1(b) shows an HAADF STEM image of the cross-sectional sample. As the contrast in this image is approximately proportional to the square of the atomic number, the ferromagnetic layers appear darker contrast than the heavy metal layers. Figure S1(c) shows compositional maps, which were recorded using EDX spectrum imaging and averaged in the horizontal direction. The different layers and elements are found in the expected sequence.

(a)

	Composition	Thickness
	Pt	2
	Ru	0.5
5×	Py	0.9
5×	Co	0.3
5×	Pt	1.5
	Pt	1.5
	Ta	3
		(nm)

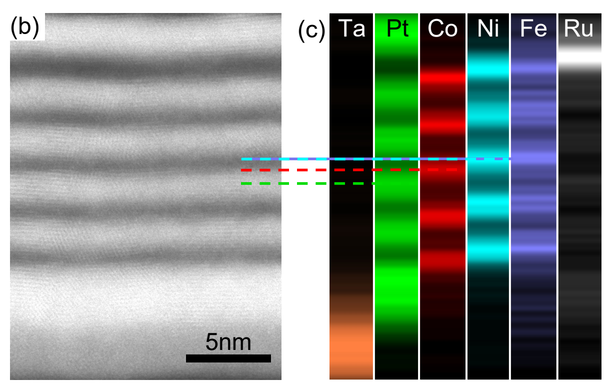

Figure S1: (a) Table showing the compositions and thicknesses (nm) of the different layers in the investigated stack. Py refers to permalloy ($Ni_{0.8}Fe_{0.2}$), while 5× refers to 5 repetitions. (b) HAADF STEM image of a cross-sectional sample of the stack. (c) Compositional maps recorded using EDX spectrum imaging and averaged in the horizontal direction. Each map provides the distribution of the indicated element projected through the sample thickness. Dashed lines are used to show the correspondence between the HAADF STEM image and compositional maps.

Supplementary Information 2:

Sample tilt series of Fresnel defocus images

In order to determine the type of magnetic texture at the domain walls, a sample tilt series of Fresnel defocus images was recorded, as shown in Fig. S2(a). The deposition of the layers onto a thin SiN membrane can induce bending deformations that modify locally the orientation of the layers with respect to the electron beam direction (McVitie et al., 2018; Fallon et al., 2019). Therefore, a particular care was taken to determine the local orientation of the layers. The zero tilt was attributed to the tilt at which the reversal of the contrast of the magnetic domain walls occurs. Fig. S2(b) shows the same series of images as in (a) but after subtraction of images recorded after magnetic saturation to remove non-magnetic background noise. Intensity profiles extracted across two 180° magnetic domain walls, along the marked arrows, are shown in Fig. S2(c). The contrast of the domain walls increases with the tilt angle for both positive and negative angles and is negligible at zero tilt, which indicates that the magnetic texture is essentially Néel-type (Benitez et al., 2015). As explained in (Fallon et al., 2019), the projection of the out-of-plane and in-plane components of the magnetic induction field at a sample tilt angle α correspond respectively to $B_S \sin(\alpha)$ and $B_S \cos(\alpha)$, where B_S is the saturation magnetic induction. The projected sample thickness is $t/\cos(\alpha)$ where t is the total thickness of the ferromagnetic layers. Therefore, the deflection of the electron beam induced by out-of-plane and in-plane components of the magnetic field is respectively proportional to $B_S t \tan(\alpha)$ and $B_S t$. For $\alpha = 10°$, the deflection induced by out-of-plane components is proportional to $B_S t \tan\alpha \approx 0.18 B_S t$. If we assume that only one of the five ferromagnetic layers of the stack is Bloch-type, then the beam deflection at zero tilt angle induced by the in-plane components of the magnetic field should be proportional to $B_S t/5 = 0.2 B_S t$. It means that if one layer of the stack is Bloch-type, then the amplitude of the domain wall contrast in the images obtained at 0° and 10° should be approximately the same. This is not the case in Fig. S2, as the domain wall contrast is stronger at 10°

compared to 0°. It can be concluded that there is no significant Bloch component in this stack. This is in agreement with previous work (Fallon et al., 2019), where Bloch components were observed in thick stacks with 10 or 15 repetitions but not in a thin stack with only 5 repetitions.

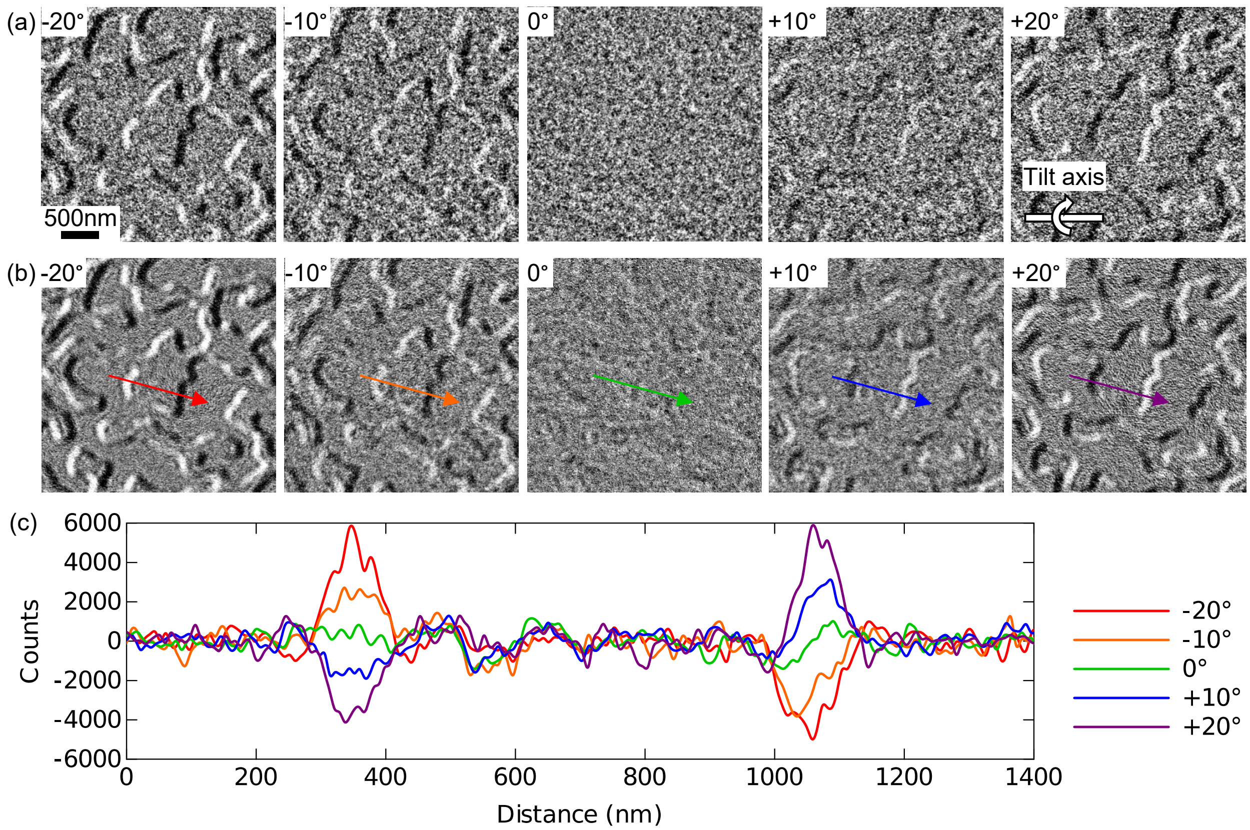

Figure S2: (a) Fresnel defocus images recorded in zero field at a defocus of -7.5 mm and the different sample tilt angles indicated on the images. (b) The same series of images as in (a) but after subtraction of background images (not shown here) recorded after magnetic saturation. (c) Intensity profiles extracted across two 180° magnetic domain walls, along the marked arrows in the images. The y axis shows both positive and negative values as a result of background subtraction.

Supplementary Information 3:

Subtraction of the non-magnetic background

Figure S3(a) shows a magnetic hysteresis curve recorded from the sample using magneto-optical Kerr effect (MOKE) microscopy in the presence of an external out-of-plane magnetic field. Figure S3(b) shows a Fresnel defocus image of several individual magnetic skyrmions recorded in the presence of an applied magnetic field of 23 mT. The red line in the image is a reference marker that was added to facilitate the observation of small changes between the images. As explained in the article, the image contains a high spatial frequency background signal, which arises primarily from the presence of diffraction contrast from small crystal grains. In order to separate the magnetic and non-magnetic contributions to the contrast, one possibility involves the acquisition of another image with the sample saturated using an applied magnetic field of 46 mT, as shown in Fig. S3(c). The orientation of the yellow line with respect to the red line indicates a rotation of the image. As a first test, these images were aligned using cross-correlation. (See script in Supplementary Information 4). The result of the subtraction is shown in Fig. S3(d). This subtraction does not improve the visibility of the skyrmions because of the slightly different magnification and rotation (approximately 1% and 2°, respectively) of the images. These differences have been corrected manually in Fig. S3(e) based on a careful visual comparison of the images. The resulting difference image, which is shown in Fig. S3(f), reveals a significant improvement in magnetic skyrmion visibility. However, the hysteresis loop in (a) shows a plateau when decreasing the applied magnetic field after saturation, meaning that the sample remains saturated even when the applied magnetic field is removed completely. Background images can therefore be recorded at lower fields after the sample has been saturated magnetically. Figure S3(g) shows another background image recorded after decreasing the applied magnetic field back to 23 mT (*i.e.*, to the same value as in (b)). The resulting difference image is shown in Fig. S3(h) after alignment using cross-correlation without changing the rotation or magnification. Figure S3(h) resembles that in

Fig. S3(f), but the noise has been reduced further.

In order to facilitate the comparison of the background noise in the images, Fourier transforms and corresponding rotational averages are shown in Fig. S3(i, j). The high frequency components (> 20 µm^{-1}) are minimized in Fig. S3(h) compared to the other images. In summary, the latter approach, in which a background image is recorded at the same value of external field as the magnetic skyrmion image, provides a relatively easy and effective method of removing non-magnetic contributions to the contrast.

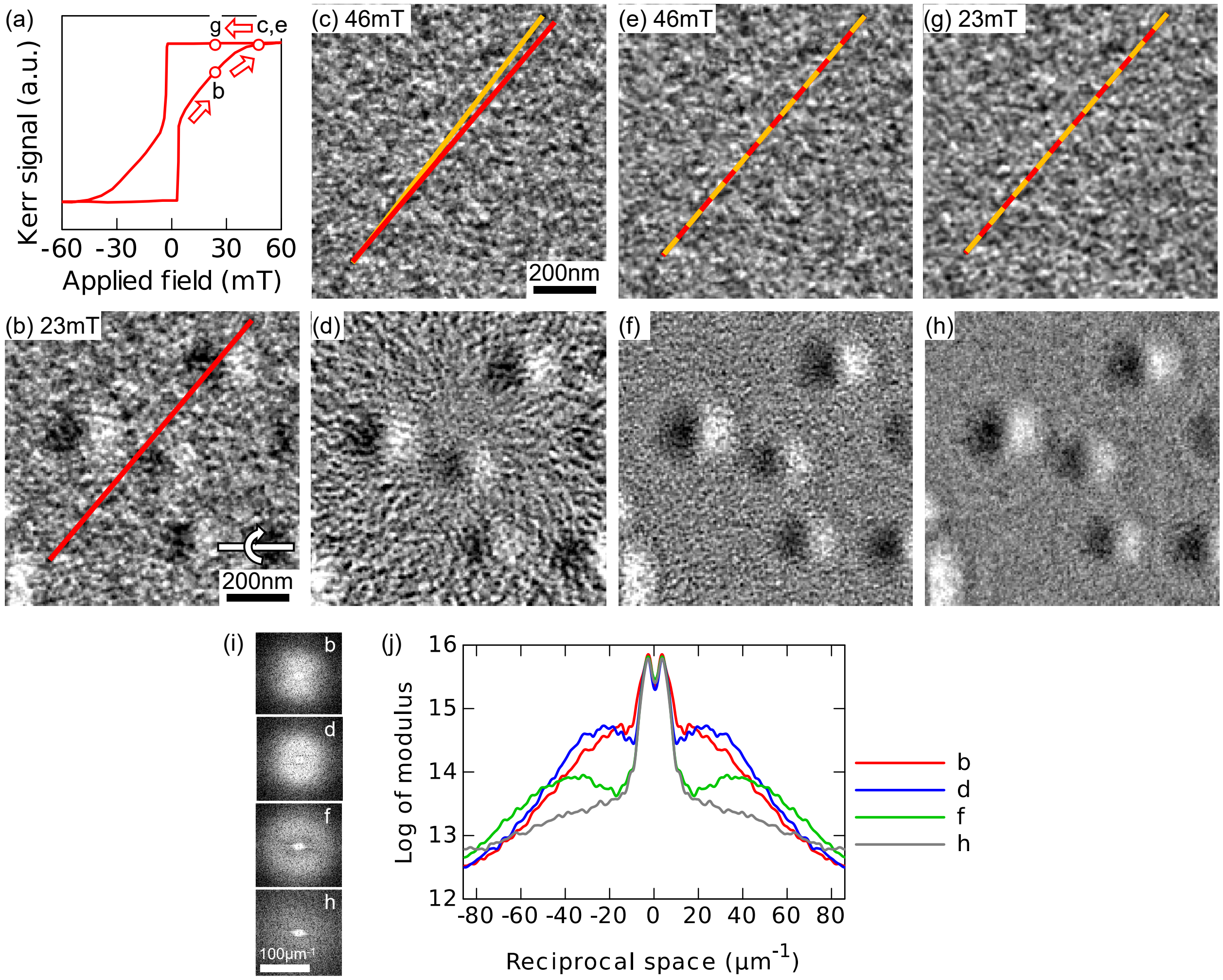

Figure S3: (a) Magnetic hysteresis loop recorded using MOKE microscopy in the presence of an out-of-plane applied magnetic field. The points on the curve correspond to recorded images. (b) Fresnel defocus image of individual magnetic skyrmions recorded in Lorentz mode at a defocus of -7.5 mm, a sample tilt angle of 30°, with an exposure time of 6 s in the presence of an applied magnetic field of 23 mT. The red line is a reference marker that was added to facilitate the observation of small changes in subsequent images. (c) Fresnel defocus image recorded with the sample at saturation in the presence of an applied magnetic field of 46 mT. The orientation of the yellow line with respect to the red line indicates rotation of the image. (d) Difference between images (b) and (c) after alignment using cross-correlation. (e) As in (c) after correction for rotation and magnification with respect to (b). (f) Difference between (b) and (e). (g) Fresnel defocus image recorded after magnetic saturation of the sample at 46 mT and then decreasing the applied magnetic field to 23 mT. (h) Difference between (b) and (g) after alignment using cross-correlation. (i) Logarithm of the modulus of the Fourier transform of each of the four images shown in (b, d, f, h). (j) Rotational averages of the Fourier transforms shown in (i).

Supplementary Information 4:

Simple cross-correlation alignment script

In order to subtract two images, alignment is necessary to compensate for drift of the sample or the image between successive acquisitions. The script below can be executed in Digital Micrograph (Gatan) software. The images should first be opened. When executing the script, a window appears and the user is prompted to select the images to be aligned. A cross-correlation is calculated and the position of the maximum is detected. The script shifts one image with respect to the other, calculates their difference and displays it.

```
image img1, img2, cross, shiftedimg2, difference
number width, height, maxx, maxy, shiftx, shifty, scalex, scaley
string unit
gettwoimages("Select images",img1,img2)
getsize(img1,width,height)
getscale(img1,scalex,scaley)
getunitstring(img1,unit)
cross=crosscorrelate(img1,img2)
max(cross,maxx,maxy)
shiftx=(maxx-width/2)
shifty=(maxy-height/2)
shiftedimg2=img2*0
shiftedimg2=warp(img2,icol-shiftx,irow-shifty)
difference=img1-shiftedimg2
setname(difference,"Difference")
setscale(difference,scalex,scaley)
setunitstring(difference,unit)
showimage(difference)
```

Supplementary Information 5:

Background subtraction in applied field series

In order to demonstrate further the applicability of the background subtraction procedure described in the article, series of Fresnel defocus images were recorded in the presence of different applied magnetic fields. The hysteresis curve shown in Fig S4(a) summarizes the procedure that was used. A first series of magnetic skyrmion images was recorded in a range of applied magnetic fields from 0 to 37 mT (blue points) and the sample was saturated magnetically with a field of 46 mT. A series of background images was then collected (green points) at the same applied magnetic field values as the first series, but in reverse order. Figure S4(b) shows the original series of magnetic skyrmion images. The magnetic skyrmion size and density decrease with increasing applied magnetic field. Figure S4(c) shows a corresponding series of images after alignment and subtraction of the background images (not shown). For all of the applied magnetic field values in this range, background subtraction reduces the noise and improves the visibility of the magnetic skyrmions significantly.

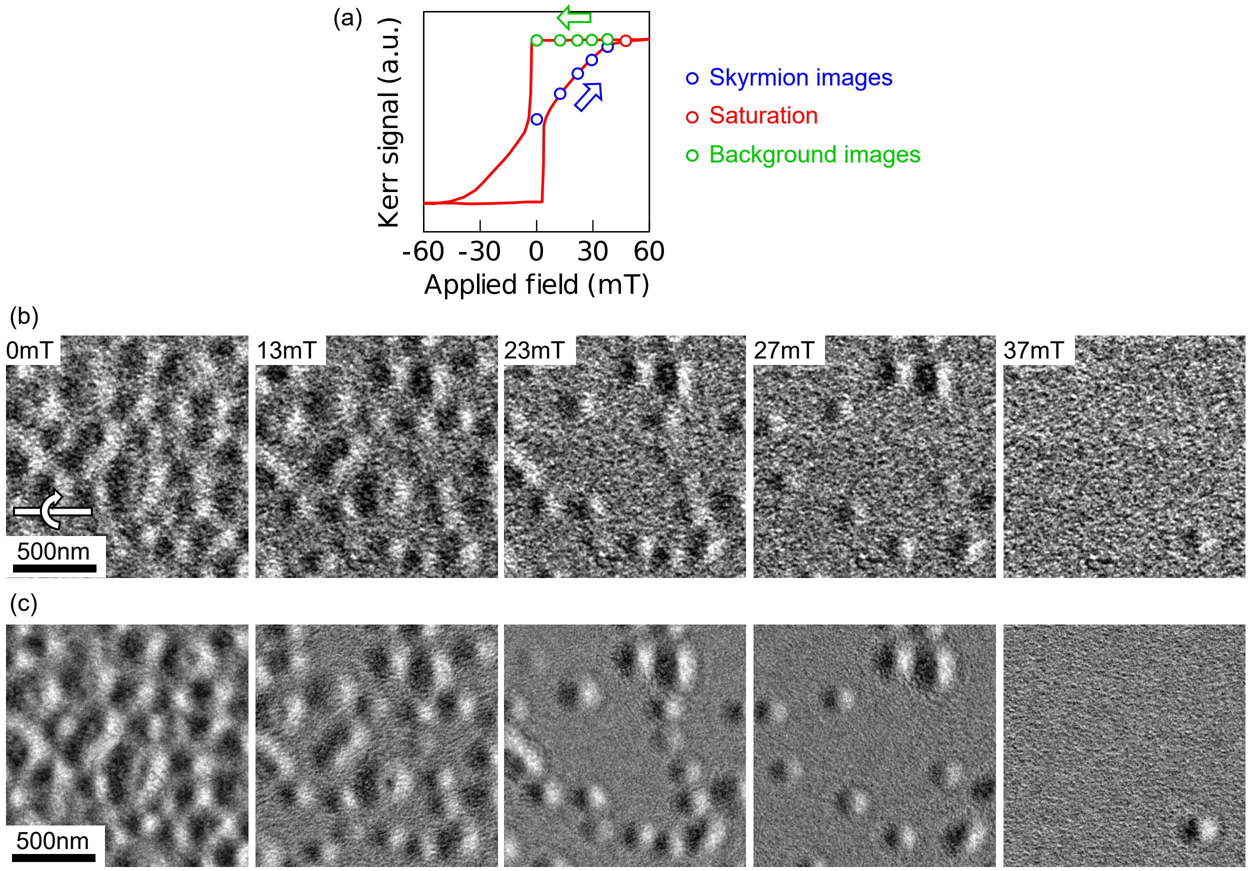

Figure S4: (a) Magnetic hysteresis loop recorded using MOKE in the presence of an applied out-of-plane magnetic field. The points on the curve correspond to recorded images. (b) Fresnel defocus images recorded at a defocus value of -7.5 mm and a sample tilt angle of 30° in the presence of the different applied magnetic fields indicated on the images. The position of each image is indicated by a blue point on the hysteresis curve in (a). (c) The same series of images as in (b), but after subtraction of background images (not shown). The position of each image is indicated by a green point on the hysteresis curve in (a).

Supplementary Information 6: Measurement of magnetic domain wall width using off-axis electron holography

Off-axis electron holography was used to measure the widths of the magnetic domain walls. One advantage of using this technique over Fresnel defocus imaging is that the image is recorded in-focus and the magnetic domain wall width can be measured directly without interpolation. Off-axis electron holography (Denneulin et al., 2021) was carried out in Lorentz mode using the same microscope that was used for Fresnel defocus imaging (described in the main article). A focused ion beam workstation was first used to mill away part of the SiN membrane, in order to create a vacuum reference region. A single post-specimen electron biprism was used to overlap a reference wave travelling in vacuum with an object wave passing through the sample. Elliptical illumination was used to optimize the coherence of the beam in the direction perpendicular to the biprism. The biprism voltage was set to 124 V, resulting in a holographic ovelap width of 2.7 µm and a holographic interference fringe spacing of 2.3 nm. Wave function reconstruction was carried out using the Holoworks plugin (Voelkl & Tang, 2010) in Digital Micrograph software (Gatan). The spatial resolution in the phase images was 7 nm (determined by the size of the aperture used in Fourier space). Figure S5(a) shows a raw phase image of two 180° magnetic domain walls recorded in zero field. Figure S5(b) shows a background-subtracted phase image, from which non-magnetic contributions to the phase have been removed by subtracting a second phase image obtained after magnetic saturation (using the same method that was used for Fresnel defocus images). Figure S5(c) shows the corresponding phase gradient in the horizontal direction, which is proportional to the vertical component of the projected magnetic induction field. Figure S5(d) shows a profile extracted in a direction perpendicular to the magnetic domain walls. In order to reduce noise, the profile was averaged along the vertical direction (parallel to the magnetic domain walls) over a distance of 200 nm. The profile was fitted using two *tanh* functions, which are also shown in Fig. S5(d). The functions are defined by the expression $y = y_0 + a \tanh((x - x_0)/w)$, where y_0, a, x_0 and w are constants obtained from the fitting procedure. For both magnetic domain walls, the fit was found to converge for $w = 6$ nm. The width of the magnetic domain wall can then be defined (Jiles, 2015) as $\pi w = 19 \pm 7$ nm, where the stated precision corresponds to the spatial resolution of the phase image.

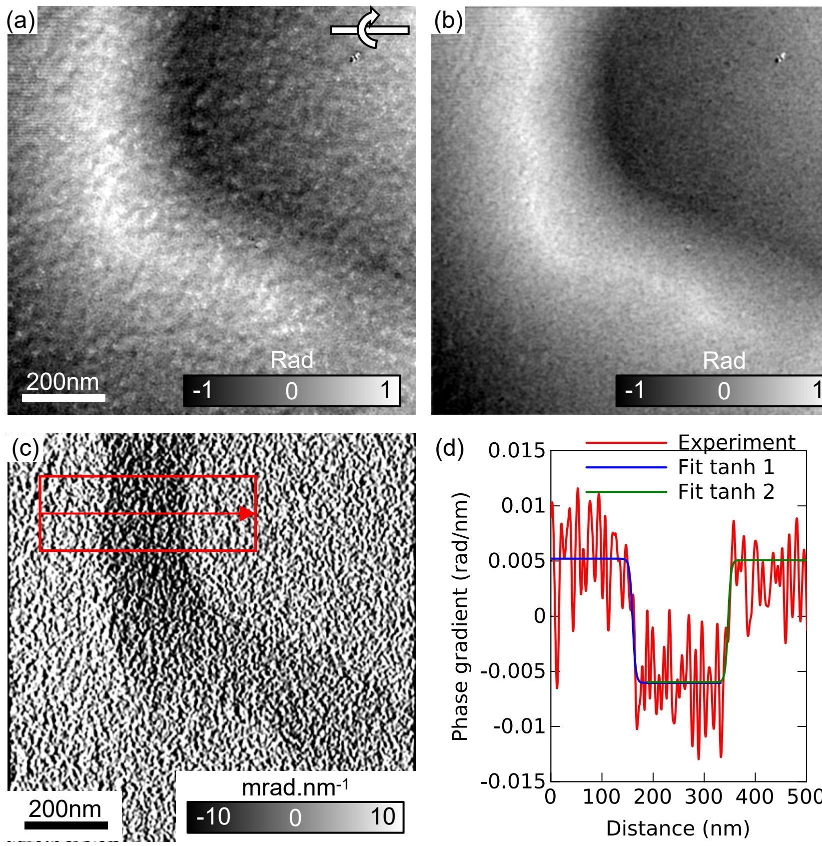

Figure S5: (a) Electron optical phase image of two 180° magnetic domain walls recorded using off-axis electron holography. The image was recorded at a sample tilt angle of 20° in zero field. (b) The same image after background subtraction. (c) Phase gradient calculated in the horizontal direction. (d) Line profile extracted from the region marked by a red box in (c), in a direction perpendicular to the magnetic domain walls. The line profile was averaged over a distance of 200 nm in parallel to the magnetic domain walls to reduce noise and was fitted using two *tanh* functions to estimate the widths of the magnetic domain walls.

Supplementary Information 7: Influence of a small Bloch component in simulated Fresnel images

It was previously reported that thick multilayer samples can host hybrid Bloch-Néel domain walls (with up to 18% Bloch-type components in a 15×Co/Ru/Pt sample (Fallon et al., 2019)). Although the Bloch components are not significant in the sample investigated here (see Supplementary Information 2), additional simulations have been performed to understand their possible influence on the apparent size of small skyrmions. Figure S6(a) shows the magnetization field of a 50 nm pure Néel-type magnetic skyrmion observed at a sample tilt angle of 20° (with the tilt axis horizontal) calculated using the analytical expression given in the main article. Figure S6(b) shows the corresponding magnetization field of a 50 nm mixed Bloch-Néel-type skyrmion with 20% Bloch components. Figure S6(c) shows a series of Fresnel images calculated from the model (a) for a defocus range of 100 µm to 2 mm. As explained in the article, at a low defocus value (100 µm), the apparent magnetic skyrmion size (*i.e.* the distance between the dip and peak in intensity) matches the effective magnetic skyrmion size (50 nm). At intermediate defocus values (for example 700 µm), the size is underestimated (36 nm), as the Fresnel fringes from opposites sides of the magnetic skyrmion overlap. At larger defocus values (2 mm), the size is overestimated (66 nm). Figure S6(d) shows a corresponding series of Fresnel images calculated from the model (b). The presence of Bloch components induces a slight asymmetry in the contrast and the peak and the dip are both slightly shifted to the right side of the image. However, globally the apparent sizes of the skyrmion are nearly the same as previous (only the value measured at 500 µm defocus is slightly different with 41 nm instead of 45 nm).

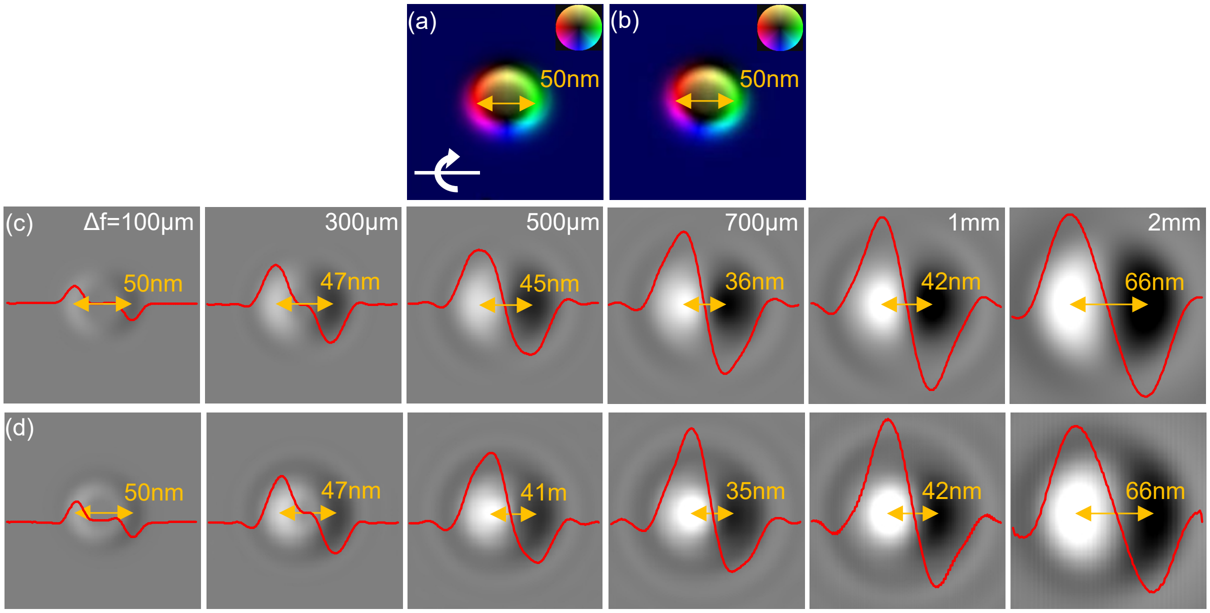

Figure S6: (a) Theoretical magnetization distribution of a 50 nm pure Néel-type skyrmion for a sample tilt angle of 20° (with the tilt axis horizontal). The direction of the magnetization projected in the image plane is given by the colour wheel in the upper right corner. (b) Theoretical magnetization distribution of a 50 nm mixed Bloch-Néel-type skyrmion with 20% Bloch components for a sample tilt angle of 20°. (c) Simulated Fresnel defocus images calculated from the model shown in (a) for the different defocus values indicated in the images. The red curves correspond to intensity profiles in the horizontal radial direction. The apparent size, *i.e.* the distance between the peak and the dip, is indicated on each image. (d) Simulated Fresnel defocus images calculated from the model shown in (b).

Supplementary Information 8:

Influence of the beam divergence in simulated Fresnel images

As explained in Appendix of the article, Fresnel defocus images were calculated from a simulated phase image $\varphi_{\text{mag}}(x, y)$ by setting up a wave function of the form $\Psi(x, y) = e^{i\varphi_{\text{mag}}(x,y)}$, which was modified in Fourier space according to the expression

$$\Psi_{\text{LTEM}}(x, y) = \mathcal{F}_2^{-1}\left\{\mathcal{F}_2\left\{e^{i\varphi_{\text{mag}}(x,y)}\right\} \cdot e^{-i\chi(q_x,q_y)} \cdot E(q_x, q_y)\right\} , \tag{1}$$

where $\mathcal{F}_2\{...\}$ and $\mathcal{F}_2^{-1}\{...\}$ denote a two-dimensional Fourier transform and its inverse. $\chi(q_x, q_y)$ denotes an aberration function, which takes the form (Chapman, 1984)

$$\chi(q) = \pi\lambda\Delta f q^2 + \frac{\pi}{2}C_S\lambda^3q^4 , \tag{2}$$

where $q = \sqrt{(q_x^2 + q_y^2)}$, λ is the wavelength, Δf is the defocus and C_S is the spherical aberration coefficient of the Lorentz lens. The C_S value of a Lorentz lens can be approximately 10 m but its influence on the aberration function is negligible compared to the defocus term because of the large defocus values (hundreds of microns) used for magnetic imaging (Nuhfer et al., 2010). E in equation (1) is a damping envelope, which allows taking into account the spatial coherence of the electron source and can be defined (Walton et al., 2013)

$$E(q) = \exp\left[-\left(\frac{\pi\alpha}{\lambda}\right)^2\left(C_S\lambda^3q^3 + \Delta f\lambda q\right)^2\right] , \tag{3}$$

where α is the beam divergence angle. $\alpha = 0$ corresponds to a fully coherent wave. In reality, α can be approximately 100 µrad for a thermionic source and less than 10 µrad for a field-emission gun (Reimer & Kohl, 2008).

Figure S7(a) shows simulated Fresnel defocus images of a 50 nm Néel-type magnetic skyrmion for a defocus of 300 µm and for three different values of the beam divergence angle $\alpha = 0$, 10 and 100 µrad. Figure S7(b) shows the ratio between the apparent size (distance between the peak and the dip) and the effective skyrmion size (50 nm) as a function of defocus and for three different divergence angles. The Fresnel images calculated for $\alpha = 0$ and 10 µrad are almost the same and the ratio of the apparent to effective size show a similar trend as a function of defocus. It shows that the beam divergence can be ignored in this study because a field-emission gun was used. On the other hand, if $\alpha = 100$ µrad, the intensity of the Fresnel fringes in the corresponding simulated image is strongly reduced and the apparent skyrmion size is also different. The slope of the corresponding curve in Fig S7(b) is much steeper compared to the other curves.

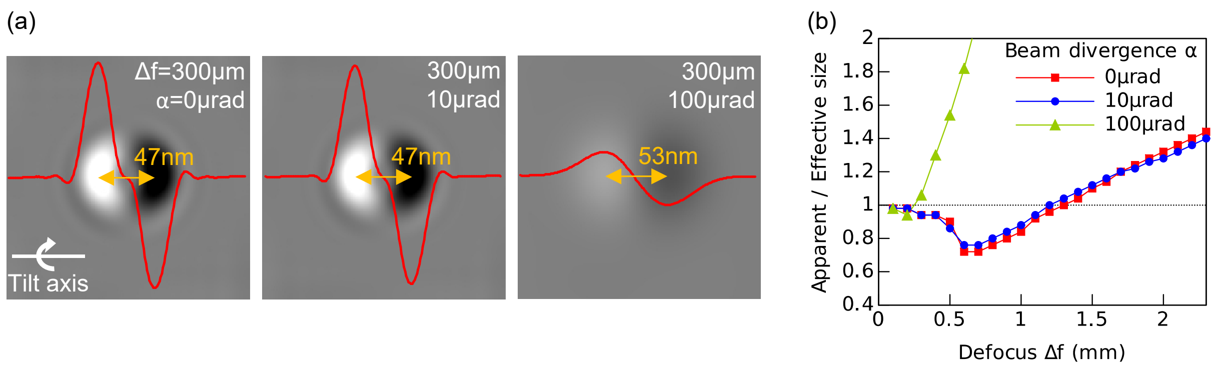

Figure S7: (a) Simulated Fresnel defocus images of a 50 nm Néel-type magnetic skyrmion for a sample tilt angle of 20° (with the tilt axis horizontal), a defocus of 300 µm and for three different beam divergence angles indicated on the images ($\alpha = 0$, 10 and 100 µrad). The red curves correspond to intensity profiles in the horizontal radial direction. The apparent size, *i.e.* the distance between the peak and the dip, is indicated on each image. (b) Ratio between the apparent size and the effective size of a 50 nm magnetic skyrmion plotted as a function of defocus for three different beam divergence angles.

References

Benitez, M.J., Hrabec, A., Mihai, A.P., Moore, T.A., Burnell, G., McGrouther, D., Marrows, C.H. & McVitie, S. (2015). Magnetic microscopy and topological stability of homochiral Néel domain walls in a Pt/Co/AlO_x trilayer, *Nat Commun* **6**, 8957, URL https://www.nature.com/articles/ncomms9957.

Chapman, J.N. (1984). The investigation of magnetic domain structures in thin foils by electron microscopy, *J Phys D: Appl Phys* **17**, 623–647, URL https://iopscience.iop.org/article/10.1088/0022-3727/17/4/003.

Denneulin, T., Caron, J., Hoffmann, M., Lin, M., Tan, H.K., Kovács, A., Blügel, S. & Dunin-Borkowski, R.E. (2021). Off-axis electron holography of Néel-type skyrmions in multilayers of heavy metals and ferromagnets, *Ultramicroscopy* **220**, 113155, URL http://www.sciencedirect.com/science/article/pii/S0304399120303004.

Fallon, K., McVitie, S., Legrand, W., Ajejas, F., Maccariello, D., Collin, S., Cros, V. & Reyren, N. (2019). Quantitative imaging of hybrid chiral spin textures in magnetic multilayer systems by Lorentz microscopy, *Phys Rev B* **100**, 214431, URL https://link.aps.org/doi/10.1103/PhysRevB.100.214431.

Jiles, D.C. (2015). *Introduction to Magnetism and Magnetic Materials, 3rd Edition*, CRC Press, URL https://www.taylorfrancis.com/books/9780429160097.

McVitie, S., Hughes, S., Fallon, K., McFadzean, S., McGrouther, D., Krajnak, M., Legrand, W., Maccariello, D., Collin, S., Garcia, K., Reyren, N., Cros, V., Fert, A., Zeissler, K. & Marrows, C.H. (2018). A transmission electron microscope study of Néel skyrmion magnetic textures in multilayer thin film systems with large interfacial chiral interaction, *Sci Rep* **8**, 5703, URL https://www.nature.com/articles/s41598-018-23799-0.

Nuhfer, N.T., Budruk, A. & De Graef, M. (2010). Aberration-corrected Lorentz microscopy, *Microsc Microanal* **16**, 142–143, URL https://www.cambridge.org/core/journals/microscopy-and-microanalysis/article/aberrationcorrected-lorentz-microscopy/D4119D1ED0C2181AD67BCC44425EF006.

Reimer, L. & Kohl, H. (2008). *Transmission Electron Microscopy*, chap. Introduction, 1–15, New York, NY: Springer New York, URL https://link.springer.com/chapter/10.1007/978-0-387-40093-8_1.

Voelkl, E. & Tang, D. (2010). Approaching routine $2\pi/1000$ phase resolution for off-axis type holography, *Ultramicroscopy* **110**, 447–459, URL http://www.sciencedirect.com/science/article/pii/S0304399109002629, Hannes Lichte 65th Birthday.

Walton, S.K., Zeissler, K., Branford, W.R. & Felton, S. (2013). MALTS: A tool to simulate Lorentz transmission electron microscopy from micromagnetic simulations, *IEEE Trans Magn* **49**, 4795–4800, URL https://ieeexplore.ieee.org/document/6461943.